Green Chemical Technology

SCIEPublish

Article

Influence Mechanisms of Particle Migration and Solution Seepage on the Leaching Process of Weathered Crust Elution-Deposited Rare Earth Ore

Wendou Chen [1,2], Zhenyue Zhang [2], Ru'an Chi [1,2], Defeng Liu [2], Zhuo Chen [2,*], Yuhe Ran [1] and Shaoping Li [1]

[1] Hubei Three Gorges Laboratory, Yichang 443007, China; chenwendou@hbsxsys.com (W.C.); rac7628@126.com (R.C.); ranyuhe@hbsxsys.com (Y.R.); lishaoping@hbsxsys.com (S.L.)
[2] Key Laboratory for Green Chemical Process of Ministry of Education, Wuhan Institute of Technology, Wuhan 430074, China; zyzxmu@wit.edu.cn (Z.Z.); liudefengoopp@126.com (D.L.)

* Corresponding author. E-mail: 23051105@wit.edu.cn (Z.C.)

Received: 2 June 2026; Revised: 10 August 2026; Accepted: 1 September 2026; Available online: 15 September 2026

ABSTRACT: This study investigated the evolution of particle migration and solution seepage caused by clay mineral swelling during the leaching of weathered crust elution-deposited rare earth ore. Column leaching experiments, high-resolution X-ray computed tomography (CT), and Avizo-based seepage simulations were conducted using a composite lixiviant consisting of composite diethylenetriamine-acetate lixiviant (CDETA) (0.2 mol/L ammonium acetate and 1.0 wt% diethylenetriamine). The pore structure, particle migration, seepage velocity, and pore pressure were systematically analyzed before and after leaching. Results showed that fine particles migrated downward under seepage forces. Consequently, in the upper layer, the average pore count increased from 13,362 (raw ore) to 19,160 (leached ore), and the overall average porosity of the ore body rose from 13.04% to 19.78%. The number of pore throats in the leached ore decreased from 19,387 to 16,502 due to particle blockage. The average seepage velocity dropped from 3.50×10^{-6} m/s to 1.90×10^{-6} m/s. Pore pressure was higher in the upper layer (3859–4128 Pa) than in the lower layer (3517–3824 Pa). These changes weakened the internal pore connectivity of the ore body and intensified the local pressure gradient, which are important triggers for clay swelling and landslide hazards. This study reveals the coupling mechanism among particle migration, swelling, and seepage. The findings provide a theoretical basis for optimizing lixiviant injection, inhibiting particle migration, and ensuring mine safety.

Keywords: Weathered crust elution-deposited rare earth ore; Clay minerals; Particle migration; Solution seepage; Pore structure

1. Introduction

Weathered crust elution-deposited rare earth ore (ion-adsorption rare earth ore) is an extremely important strategic mineral resource in China. It is rich in medium and heavy rare earth elements, which are widely used in new energy, national defense technology, and high-end manufacturing [1,2]. Currently, the *in-situ* leaching is the main extraction method. In this process, a leaching solution is injected to exchange rare earth ions adsorbed on clay mineral surfaces into the solution, followed by collection [3]. However, during *in-situ* leaching, the large injection of leaching solution can cause hydration swelling of clay minerals [4]. This reduces the interparticle cohesion. Meanwhile, fine particles migrate under seepage forces, blocking pore channels and altering the pore structure and seepage characteristics of the ore body [5–7]. These changes decrease rare earth recovery efficiency and increase the risk of geological hazards such as landslides.

Numerous studies have examined clay mineral swelling during the leaching of weathered crust elution-deposited rare earth ore. Zhang et al. [8] investigated the effect of ammonium salt lixiviant on clay swelling. They found that NH_4^+ can compress the thickness of the electrical double layer, thereby inhibiting swelling. Zhou et al. [9] used nuclear magnetic resonance (NMR) and other techniques to explore the evolution of pore structure in ore samples during leaching with cations of different valences. Their results showed that ion exchange reactions caused downward migration of fine solid particles. Dynamic transformation of these particles on pore surfaces led to significant changes in the proportion of pores of different sizes. Regarding particle migration and seepage characteristics, Luo et al. [10] observed through experiments that fine particle movement during leaching alters ore permeability. Wang et al. [11] monitored changes in pore size distribution of ore samples using NMR. They confirmed the blocking effect of fine particle migration on micropores. Dianyu et al. [12] analyzed the influence of particle transport on pore connectivity via numerical simulation. They pointed out that particle deposition locations significantly affect local seepage pathways. However, most existing studies have focused on single-salt lixiviants and relied on indirect methods such as NMR and permeability tests, which cannot provide direct three-dimensional visualization or quantitative pore-scale evidence. Consequently, the coupled mechanisms among particle migration, swelling, and seepage remain poorly understood.

In recent years, the combination of high-resolution X-ray computed tomography (CT) and three-dimensional reconstruction software (e.g., Avizo) has provided a powerful tool for detailed characterization of pore structures in porous media and for seepage simulation [13,14]. This approach has been applied to study seepage properties in oil and gas reservoir rocks such as shale and sandstone [15,16]. However, its use in the leaching process of weathered crust elution-deposited rare earth ore is still in the early stages. In this study, we selected a weathered crust elution-deposited rare earth ore from Lincang, Yunnan Province and applied a combination of column leaching, high-resolution 3D CT scanning, and Avizo-based seepage simulation. This approach enables quantitative 3D visualization of pore structure evolution, seepage velocity, and pore pressure, directly revealing the coupled effects of particle migration and swelling on seepage behavior. The results provide a basis for optimizing lixiviant injection and mitigating landslide risks.

2. Materials and Methods

2.1. Experimental Materials

Ore samples were collected from the full weathering layer of a weathered crust elution-deposited rare earth ore in Lincang, Yunnan Province, China. The samples were dried and sieved before use. The full particle size distribution analysis of the ore sample is shown in Figure 1. Figure 1b presents the particle size distribution of the −0.106 mm ore fraction from the sample shown in Figure 1a. In the overall sample, coarse particles (+0.85 mm) account for 31.67%, while fine particles (−0.106 mm) account for 25.91%. Together, these two size fractions make up more than half of the total sample, at 57.58%. The intermediate particle size range (+0.106 ~ −0.85 mm) accounts for 42.42%, and the median particle size is approximately 0.32 mm.

The main chemical composition (by XRF) was as follows SiO_2 67.185%, Al_2O_3 22.358%, REO 0.149%, FeO 2.236%, and K_2O 4.569%. The relative contents of clay minerals (by XRD) were halloysite

67.39%, kaolinite 20.05%, illite 10.64%, and smectite 1.92%. The ion-exchangeable rare earth fraction accounted for 73.83% of the total REO. The composite lixiviant, CDETA, was formulated with 0.2 mol/L ammonium acetate (CH_3COONH_4) and 1.0 wt% diethylenetriamine (DETA).

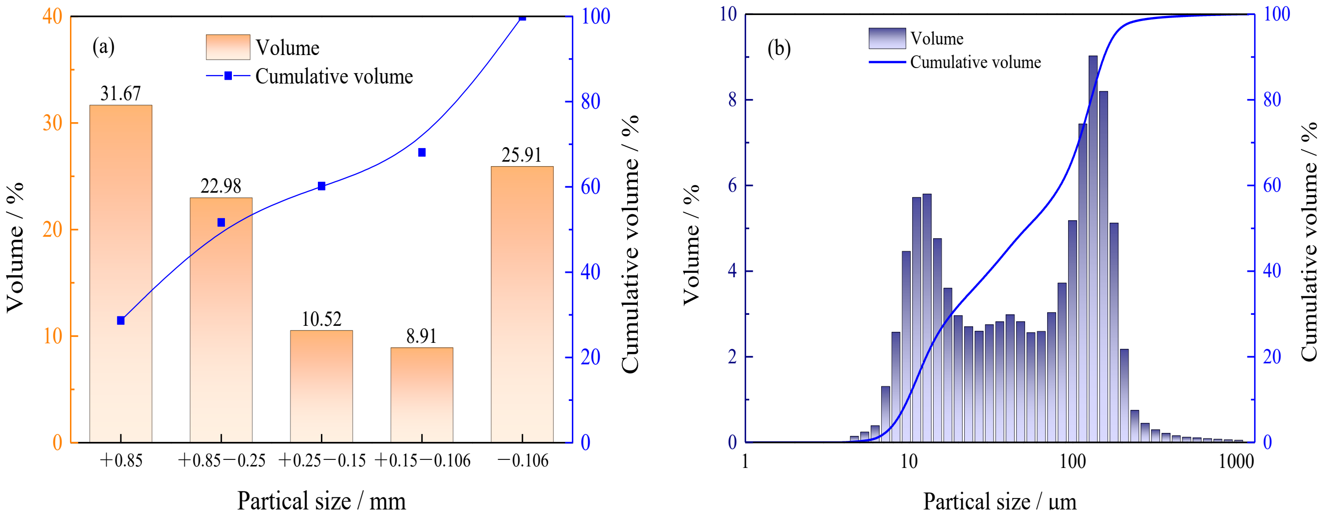

Figure 1. Particle size distribution characteristics of ore samples. (**a**) particle size distribution of the overall ore sample; (**b**) particle size distribution of the −0.106 mm ore fraction from the sample shown in (**a**).

2.2. Column Leaching Experiment

The column leaching apparatus is shown in Figure 2. Approximately 500 g of dried ore sample (obtained by quartering) was loaded into a glass column (50 mm i.d., 300 mm height), forming an ore bed of about 200 mm with a bulk density of approximately 1.35 g/cm^3. The CDETA lixiviant was injected from the top via a peristaltic pump at a flow rate of 0.5 mL/min, and the leachate was collected at the bottom. The leaching experiment was conducted at a liquid-to-solid ratio of 4:1 (mL/g) at room temperature (25 ± 2 °C). The leaching process was considered complete when no liquid further drained from the bottom of the column (total leaching duration: approximately 12 h; total lixiviant volume: 2.0 L; collected leachate volume: approximately 1.8 L), at which point the leached ores were sampled from the upper, middle, and lower layers for subsequent CT scanning. All leaching experiments were performed in triplicate using three parallel columns under identical conditions.

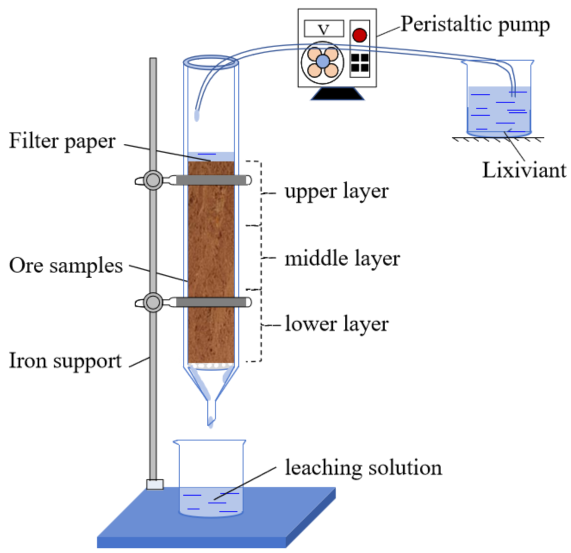

Figure 2. Rare earth column leaching apparatus.

2.3. CT Scanning and 3D Reconstruction

Raw ore and leached ore samples from three layers (upper, middle, lower) were scanned using a Geoscan 200 X-ray 3D CT scanner [17] (Tianjin Sanying Precision Instruments Co., Ltd., Tianjin, China). The CT scanning was performed at room temperature (25 ± 1 °C) with a rotation step of 0.5° per projection. Scanning parameters: voltage 130 kV, current 130 μA, spatial resolution 56 μm, full-angle rotation. For each sample, 500 two-dimensional slice images (1900 × 1900 pixels each) were obtained. The reconstructed voxel size was set to 56 μm, consistent with the scanning resolution. Image processing was performed with Avizo 2020 software, including non-local means filtering, threshold segmentation (pores *vs.* particles), and 3D pore network reconstruction. Extracted parameters: pore number, pore volume distribution, number of pore throats, and throat radius.

2.4. Seepage Simulation and Pore Pressure Analysis

Seepage paths and pore pressure distribution were simulated by solving the Navier-Stokes equations [18] using the "Absolute Permeability Experiment Simulation" module in Avizo software. The simulations were performed under steady-state conditions using a tetrahedral mesh, with convergence achieved when residuals fell below 10^{-6}. The simulation time does not correspond to the experimental duration, as the steady-state solution represents the time-independent flow field under the specified boundary conditions. Boundary conditions: inlet pressure 1.3 MPa, outlet pressure 0 MPa, fluid dynamic viscosity 0.001 Pa·s. The inlet pressure of 1.3 MPa was chosen to match the hydraulic head applied during the column leaching experiments, corresponding to the pressure head generated by the peristaltic pump at the top of the ore bed. The fluid dynamic viscosity of 0.001 Pa·s is typical viscosity of dilute aqueous ammonium salt solutions at ambient temperature, which is consistent with the actual lixiviant used in this study. The fluid was assumed to be incompressible Newtonian with no-slip at solid walls. Outputs included the seepage velocity field and pore pressure contour map. A limitation of this simulation approach is that the pore structure used for seepage modeling was derived from post-leaching CT scanning, which represents the final state of the ore sample rather than the transient evolution during the leaching process. Consequently, the simulation results reflect steady-state flow within a static pore network and cannot capture the dynamic feedback among particle migration, pore-structure alteration, and seepage behavior that occur continuously throughout the experiment.

3. Results and Discussion

3.1. CT Image Processing and Analysis of Rare Earth Ore Samples

3.1.1. Analysis of 2D Pore Structure During Leaching

To investigate the evolution of the microscopic pore structure of the ore during rare earth leaching, the upper, middle, and lower layer samples before and after column leaching were scanned by CT. The results are shown in Figure 3.

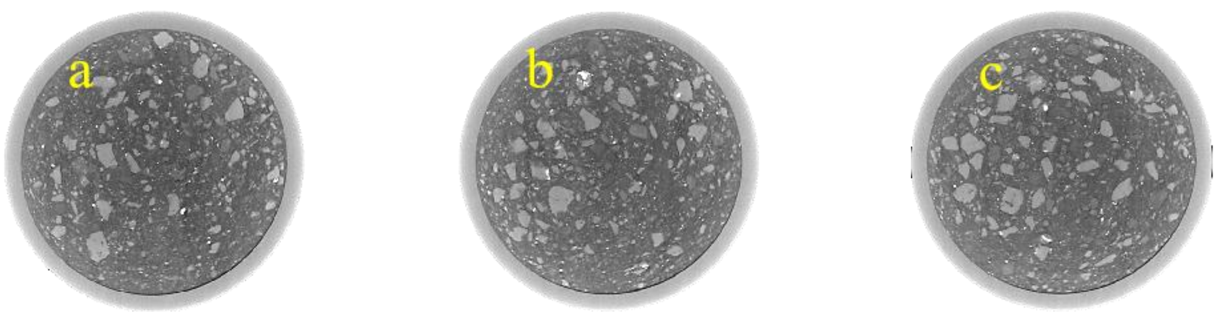

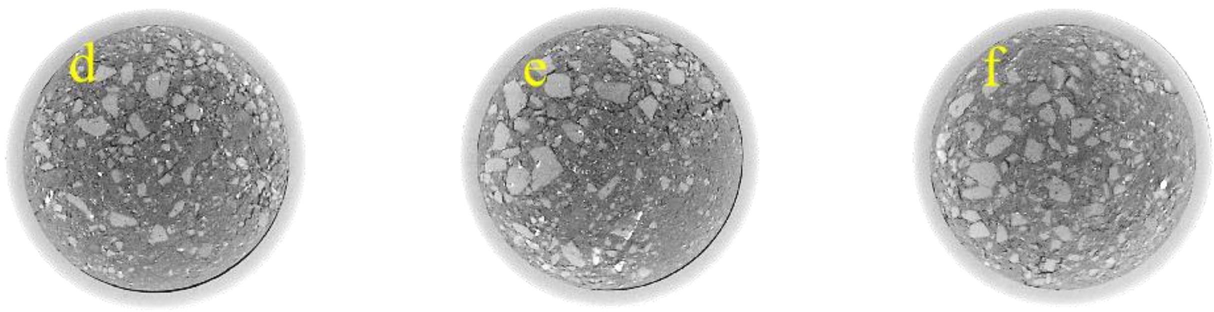

Figure 3. 2D imaging of pore structure of a rare earth ore sample. (**a**–**c**) Upper, middle, and lower layer samples of the raw ore; (**d**–**f**) Upper, middle, and lower layer samples of the leached ore.

As shown in Figure 3, fine particles in the rare earth ore samples were mostly embedded in the gaps between coarse particles. Comparing the cross-sections of raw ore and leached ore, the pore structure changed during the leaching process. Notably, pore expansion was most pronounced in the contact zones between large and fine particles, where fissures were clearly visible [19–21]. From the leached ore images, the degree of pore expansion in the upper and middle layers was considerably greater than that in the lower layer. This is because fine particles migrated downward during leaching. The reduction of fine particles in the upper layer led to pore expansion between particles. The pore expansion observed in the leached ore can be attributed to a decrease in interparticle cohesion caused by increased moisture content of the ore during leaching.

3.1.2. Three-Dimensional Pore Characteristic Analysis of Rare Earth Ore Body

Three-dimensional pore network models were reconstructed using Avizo software. Three pairs of raw ore and leached ore samples were modeled for 3D pore structure analysis. The variations in pore throat parameters and pore characteristic parameters were examined. The results are shown in Figure 4. In this figure, the ball-and-stick model represents pores (spheres) and throats (rods). Larger volumes and brighter colors indicate larger pore sizes.

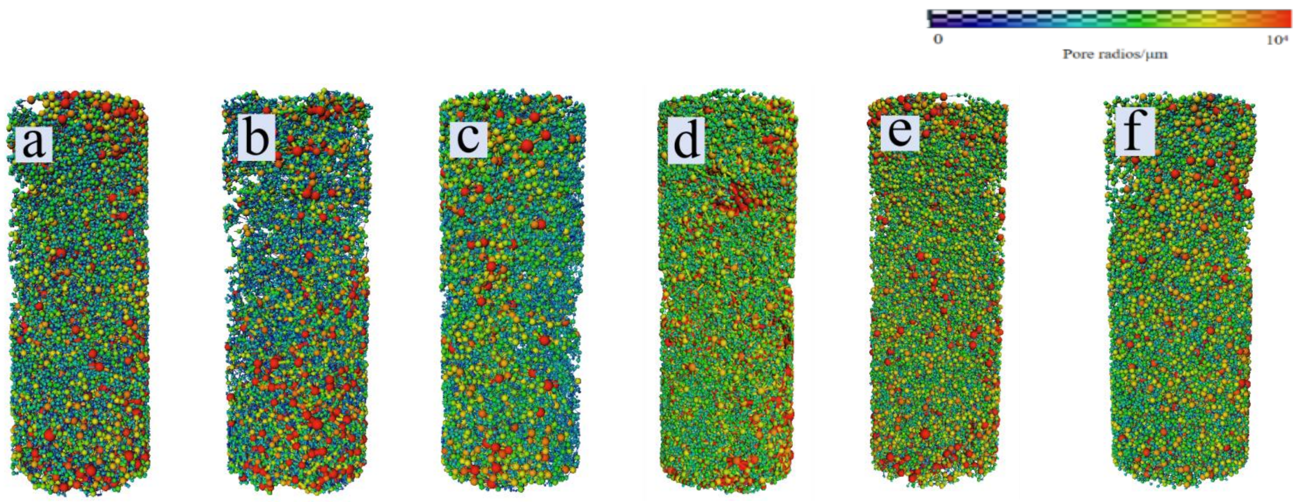

Figure 4. 3D pore model of rare earth ore sample. (**a**–**c**) 3D pore models of raw ore; (**d**–**f**) 3D pore models of leached ore.

As shown in Figure 4a–c, the pore structure of the ore body before leaching was relatively simple. Interparticle pores between large particles were well developed, providing pathways for solution seepage. The three-dimensional model exhibited a sparsely distributed ball-and-stick structure. After leaching, the number of pores increased notably. In the three-dimensional model, spheres were arranged more densely, while rods became slender and interconnected, forming a more complex pore network (Figure 4d–f). This is because the lixiviant reacted with mineral components, leading to the destruction and dissolution of mineral structures. Consequently, new pore spaces were created within the ore body. This not only increased the total porosity but also altered pore morphology and distribution [22,23]. The pore counts and volumes of the ore samples before and after leaching are summarized in Tables 1 and 2, respectively.

Table 1. Change of pore number of the rare earth ore sample.

Sample	**Pore Count**				
	Replicate 1	**Replicate 2**	**Replicate 3**	**Mean ± SD**	**Average Pore Difference**
Raw ore	13,849	13,294	12,941	13,362 ± 454	5789 ± 497
leached ore	18,517	19,414	19,547	19,160 ± 542	

Note: Data are presented as mean ± standard deviation (SD, n = 3). Replicates 1–3 represent three parallel column experiments conducted under identical conditions.

As shown in Table 1, the pore counts of all leached ore samples were higher than those of the raw ore samples. The average difference reached 5798. This indicates that the leaching process considerably increased the number of pores within the ore body. The underlying mechanism is as follows. Solution seepage acted as the primary driving force, promoting the downward migration of fine particles. Tiny particles attached to pore walls were detached, forming new pores. Meanwhile, these fine particles were carried away by the flowing leachate, further enlarging the pore space. These findings are consistent with the results of the 3D pore models shown in Figure 4.

Table 2. Pore volume distribution of rare earth ore sample (average)/μm^3.

Sample	**Average Pore Volume Distribution**									
	$10^{3–4}$	**$10^{4–5}$**	**$10^{5–6}$**	**$10^{6–7}$**	**$10^{7–8}$**	**$10^{8–9}$**	**$10^{9–10}$**	**$10^{10–11}$**	**$10^{11–12}$**	**$10^{12–13}$**
Raw ore	2165	2785	3814	1804	1161	854	505	215	51	8
leached ore	2690	3620	4948	2989	1848	1669	978	357	55	6

Table 2 shows that the pore volume distributions of the raw ore and leached ore followed similar patterns. Most pore volumes fell within the range of 10^3 to 10^{11} μm^3. The highest proportion occurred in the 10^5–10^6 μm^3 interval, representing 28.55% for the raw ore and 25.82% for the leached ore.

3.1.3. Areal Porosity Analysis of Rare Earth Ore Body

The porosity of each slice layer was calculated based on CT image processing techniques. These values were then accumulated to obtain the distribution curve of 2D porosity as a function of column height. The results are shown in Figure 5.

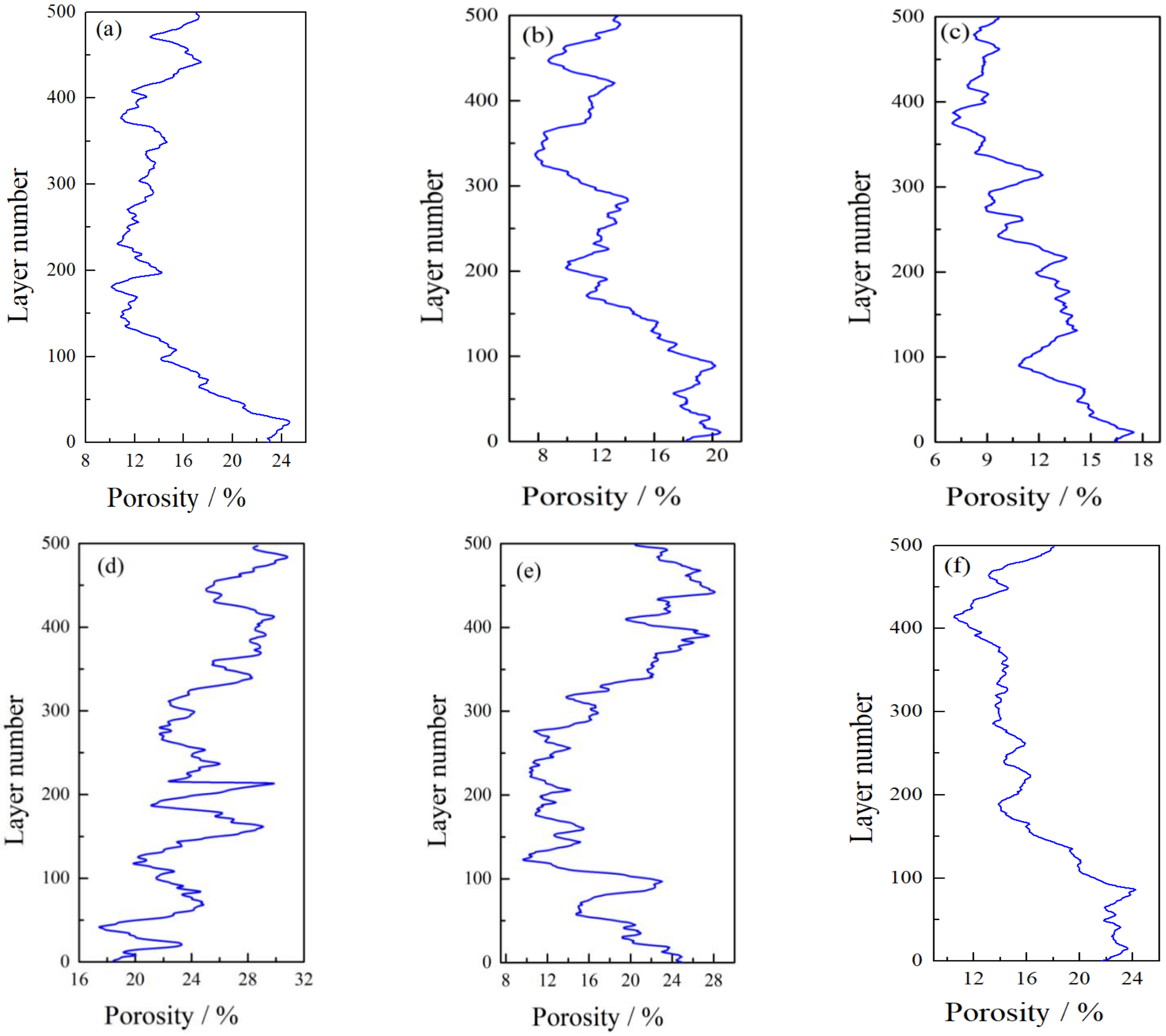

Figure 5. 2D porosity of rare earth ore sample. (**a**–**c**) 2D porosity of raw ore; (**d**–**f**) 2D porosity of leached ore.

The 2D porosity of the ore samples was unevenly distributed in the vertical direction. Before leaching, the maximum porosities of the three raw ore samples were 24.65%, 20.55%, and 17.48%, respectively. Their average porosities were 14.51%, 13.39%, and 11.21%, respectively. The overall distribution was relatively uniform. After leaching, the porosity of the leached ore samples increased in general. The maximum porosities rose to 30.84%, 28.11%, and 24.18%. The average porosities increased to 24.72%, 18.15%, and 16.46%. Notably, the increase in porosity in the upper layer was greater than in the middle and lower layers. This can be attributed to the downward migration of fine particles under the combined action of leachate infiltration and gravity. As a result, pore sizes in the upper layers expanded, leading to a higher porosity change rate.

3.1.4. Pore Throat Characteristics of the Rare Earth Ore Body

Micro-CT scanning was used to acquire images of the internal structure of the samples. The evolution of pore throats under solution seepage was analyzed. The numbers of pore throats in the ore samples before and after leaching are listed in Table 3.

Table 3. Change of pore throat quantity before and after ore leaching.

Sample	Pore Count				
	Replicate 1	Replicate 2	Replicate 3	Mean ± SD	Average Pore Throat Difference
Raw ore	19,264	18,851	20,019	19,387 ± 586	2885 + 672
leached ore	16,423	15,832	17,250	16,502 ± 710	

Note: Data are presented as mean ± standard deviation (SD, n = 3). Replicates 1–3 represent three parallel column experiments conducted under identical conditions.

The number of pore throats in the leached ore was notably lower than that in the raw ore (average difference: 2885). This is attributed to the migration of fine clay particles during leaching, which blocked some pore throats [23]. This factor critically influences the pore structure and permeability of the ore body, thereby affecting ore body stability during rare earth mining. The distribution characteristics of throat radius and throat length before and after leaching are shown in Figure 6a and Figure 6b, respectively.

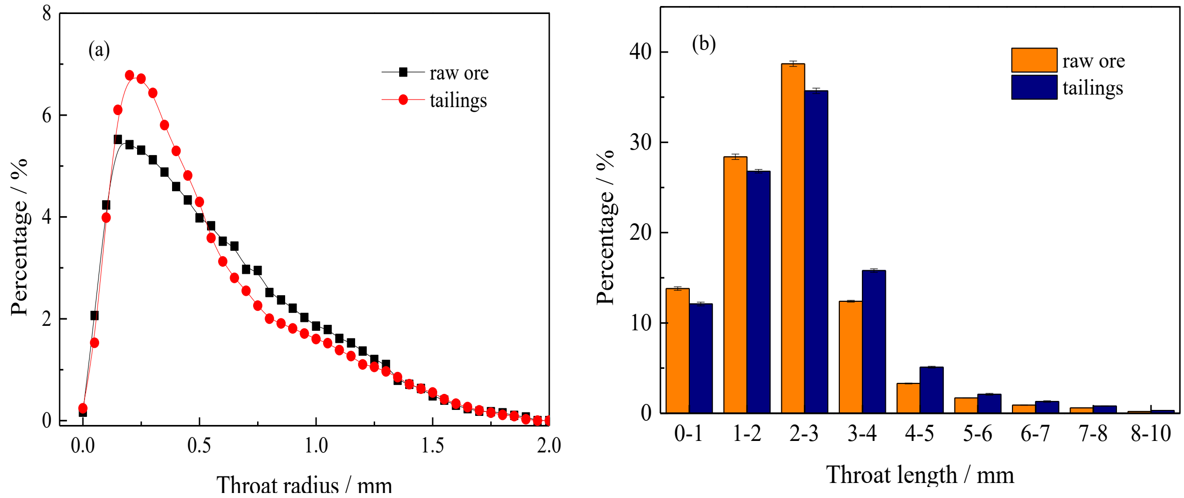

Figure 6. Distribution (average) of throat radius (**a**) and throat length (**b**) before and after leaching.

As shown in Figure 6a,b, the throat radius distribution first increased and then decreased. The proportion of pores in the 0–1 mm interval rose from 70.29% (raw ore) to 87.35% (leached ore). This indicates a decline in large pores and connectivity, along with an increase in small and medium pores. The throat length distribution also showed an initial increase followed by a decrease. Throat lengths were mainly concentrated in the range of 0–4 mm, accounting for 93.3% of the raw ore and 90.4% of the leached ore. In the 0–3 mm interval, the proportion of leached ore was lower than that of raw ore, while in the remaining intervals it was higher. These changes can be explained by the migration of fine particles with the leachate. In the upper layer, small pores decreased and large pores relatively increased, resulting in longer throats. In the lower layer, particle blockage converted large pores into small ones, increasing small pores and shortening throats [24].

3.2. Solution Seepage Distribution Characteristics During Rare Earth Leaching

Using the "Absolute Permeability Experiment Simulation" module in Avizo, the Navier-Stokes equations were solved to compare seepage simulation results of three raw ore and leached ore pairs. The seepage path distribution and average seepage velocity are presented in Figure 7 and Table 4.

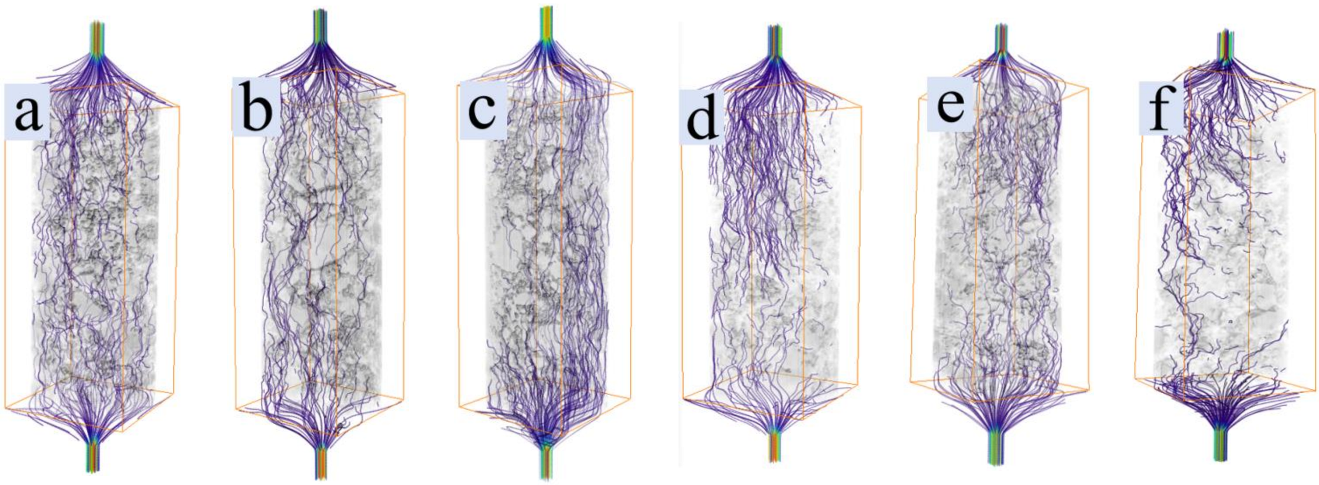

Figure 7. Characteristics of the seepage distribution of the mineral sample solution in the rare earth leaching process. (**a**–**c**) Seepage paths in raw ore; (**d**–**f**) Seepage paths in leached ore.

Table 4. Seepage velocity at different depths of ore bodies in leached ore/10^{-6} m/s.

Ore Sample	Permeability Rate			
	Replicate 1	**Replicate 2**	**Replicate 3**	**Mean ± SD**
Upper layer	2.57	2.32	2.17	2.35 ± 0.20
Middle layer	2.06	1.95	1.96	1.99 ± 0.06
Lower layer	1.58	1.61	1.71	1.63 ± 0.07
Average seepage velocity	1.96	1.88	1.86	1.90 ± 0.05

Note: Data are presented as mean ± standard deviation (SD, n = 3). Replicates 1–3 represent three parallel column experiments conducted under identical conditions.

As shown in Figure 7, the seepage paths of the solution inside the ore samples changed markedly after leaching. The streamlines were more concentrated in the upper and middle layers. In contrast, they were sparse or even discontinuous in the lower layer. In the upper layer, fine particle migration simplified the pore structure, creating wider effective channels and enhancing local pore connectivity. In the lower layer, migrating fine particles blocked pore channels, complicating the pore structure and reducing connectivity [25].

The simulated average seepage velocities of the three replicate raw ore samples were 3.58×10^{-6} m/s, 3.50×10^{-6} m/s, and 3.44×10^{-6} m/s, respectively. According to Table 4, after leaching, the average seepage velocities in the leached ore decreased to 1.96×10^{-6} m/s, 1.88×10^{-6} m/s, and 1.86×10^{-6} m/s, showing a marked reduction. Furthermore, within the same ore sample, the seepage velocity gradually decreased with increasing depth. Taking replicate 1 as an example, the velocity dropped from 2.57×10^{-6} m/s in the upper layer to 1.58×10^{-6} m/s in the lower layer. This indicates that the migration and accumulation of fine clay particles during leaching reduced inter-pore connectivity, thereby altering seepage paths and inhibiting solution permeability [26].

3.3. Pore Pressure Distribution in Ore Samples During Rare Earth Leaching

To further elucidate the mechanism underlying changes in seepage behavior, pore pressure simulations were conducted on ore samples before and after leaching. The results are presented in Figure 8 and Table 5.

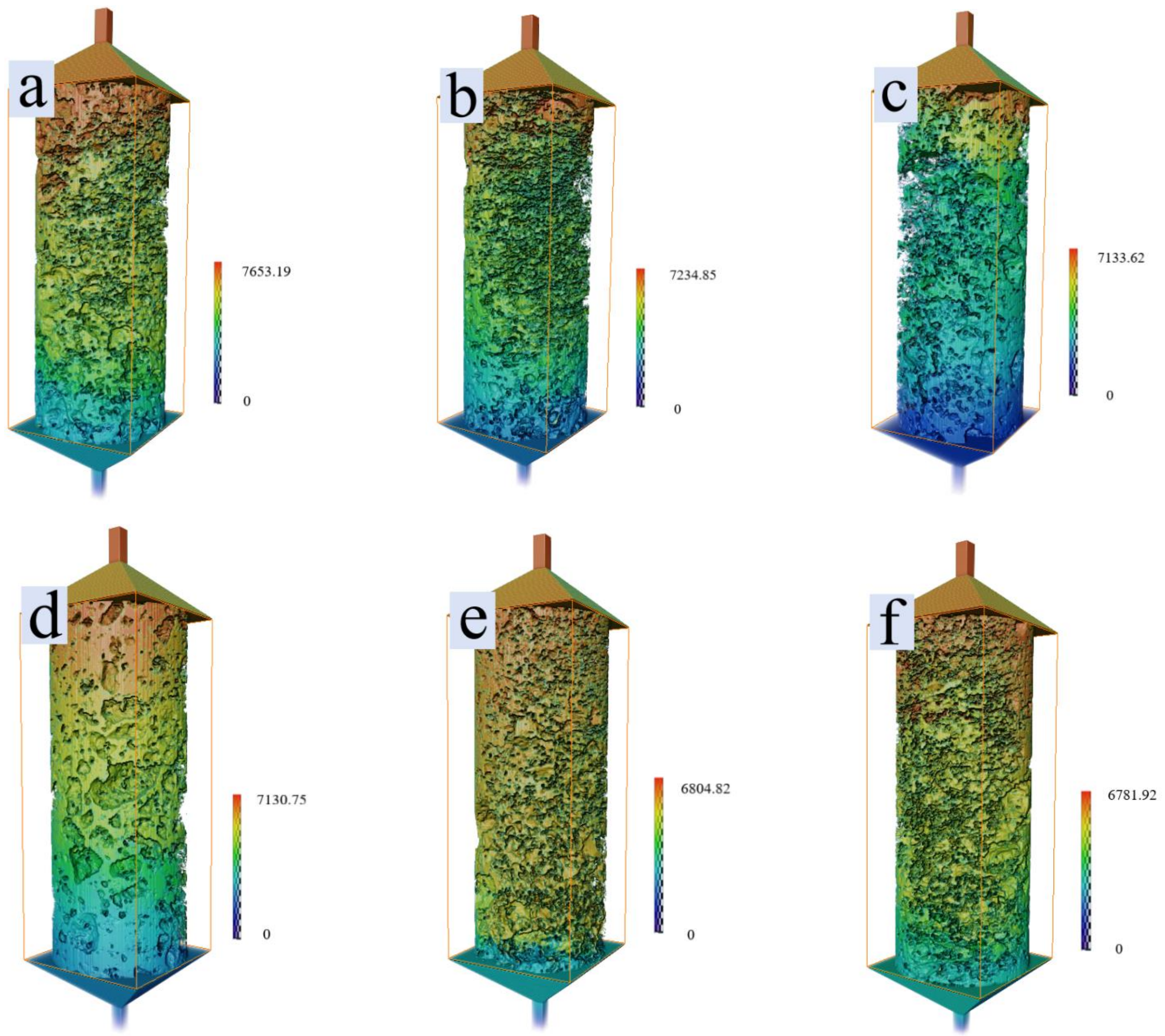

Figure 8. Pore pressure distribution of ore samples during the rare earth leaching process. (**a**–**c**) Pore pressure of raw ore; (**d**–**f**) Pore pressure of leached ore.

Table 5. Pore pressure at different depths of ore bodies in leached ore/Pa.

Ore Sample	Pore Pressure			
	Replicate 1	Replicate 2	Replicate 3	Mean ± SD
Upper layer	4128.71	4016.35	3859.89	4001.65 ± 135.12
Middle layer	3961.23	3824.19	3647.16	3810.86 ± 157.56
Lower layer	3824.65	3659.88	3517.56	3667.36 ± 154.00
Average pore pressure	3947.51	3759.62	3596.37	3767.83 ± 175.61

Note: Data are presented as mean ± standard deviation (SD, n = 3). Replicates 1–3 represent three parallel column experiments conducted under identical conditions.

As shown in Figure 8, pore pressure was highest at the solution injection point and gradually decreased along the flow direction. Before leaching, the average pore pressures of the three raw ore samples were 4253.26 Pa, 4163.84 Pa, and 3917.65 Pa, respectively. After leaching, they decreased to 3947.51 Pa, 3759.62 Pa, and 3596.37 Pa, respectively. This decreasing trend is mainly attributed to the combined effects of hydraulic gradient, matrix adsorption, and gravity, which slowed down the vertical seepage velocity of the solution [27].

According to Table 5, after leaching, the pore pressure in the upper and middle layers was markedly higher than that in the lower layer. For example, in replicate 1, the pore pressure in the upper layer was 4128.71 Pa, whereas in the lower layer it was only 3824.65 Pa. This is because fine particles migrated downward, leading to larger pore sizes and a simpler pore structure in the upper layer, thereby enhancing liquid storage capacity and increasing pressure. In contrast, particle blockage in the lower layer reduced pore sizes and complicated the pore structure, decreasing solution flow capacity and resulting in lower pore pressure. These results are consistent with the trends observed in the pore structure parameters, confirming the regulatory role of particle migration on pore pressure distribution.

3.4. Coupling Mechanism of Particle Migration, Swelling, and Seepage

During the leaching process, a coupling mechanism exists among clay mineral swelling, particle migration, and solution seepage. The schematic diagram of this mechanism is shown in Figure 9.

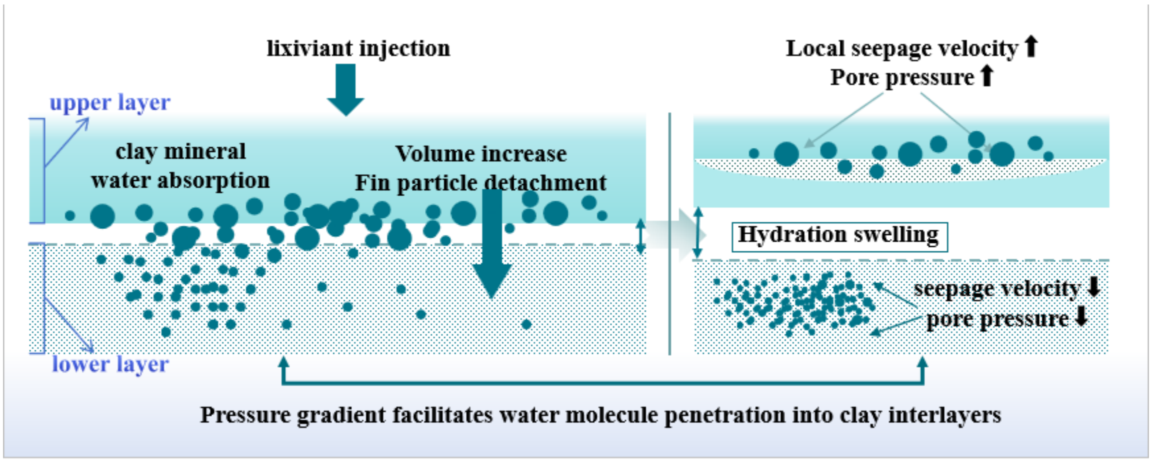

Figure 9. Schematic diagram of the coupled mechanism among clay mineral swelling, particle migration, and solution seepage in the upper and lower layers during the leaching process.

Upon lixiviant injection, clay minerals absorb water and swell, leading to an increase in volume and a decrease in interparticle cohesion. Swelling is considered to facilitate the detachment of fine particles, which are then inferred to migrate downward driven by seepage. Although clay swelling was not directly measured in this study, its occurrence is supported by multiple lines of indirect evidence. The significant increase in upper-layer porosity (from 14.51% to 24.72%, as shown in Figure 5), the reduction in pore throat number (from 19,387 to 16,502, as shown in Table 3), and the observed structural changes (as shown in Figure 3) are all consistent with the scenario in which hydration swelling weakens interparticle cohesion and promotes particle detachment. In addition, the decreased seepage velocity (Table 4) and the development of a local pore pressure gradient between the upper and lower layers (Table 5) are consistent with swelling-induced pore structure alteration that progressively inhibits solution permeability. However, it should be noted that the observed pore structure changes may also be partially attributed to particle rearrangement and mineral dissolution, which are inherent to the leaching process. While CT imaging and pore network analysis can reveal the net structural changes, they cannot fully distinguish the individual contributions of particle migration, particle rearrangement, and mineral dissolution. Nevertheless, the consistent trends of porosity increase in the upper layer, pore throat reduction in the lower layer, and the development of a pressure gradient are most reasonably explained by the combined effects of these processes, with particle migration playing a dominant role. The resulting pressure gradient between the upper and lower layers further promotes water intrusion into clay interlayers, exacerbating swelling. If this cycle is left uncontrolled, it will lead to a continuous rise in local saturation of the ore body, a decline in shear strength, and ultimately trigger landslides. Therefore, inhibiting clay swelling and reasonably controlling the injection flow rate are key measures to interrupt this vicious cycle. This particle blockage process is conceptually analogous to clogging in vadose zone infiltration systems, where particle accumulation reduces hydraulic conductivity [28]. In our system, the decreased pore throat connectivity and seepage velocity in the lower ore layers (Tables 3 and 4) similarly reflect the permeability reduction caused by fine particle migration and blockage.

4. Conclusions

During leaching, lixiviant injection is inferred to trigger hydration swelling of clay minerals. This inference is supported by the observed increase in porosity, reduction in pore throat size, structural changes, and decline in seepage velocity, which are consistent with swelling-induced structural alteration. Fine particles are inferred to migrate significantly downward under seepage forces, as supported by the observed porosity and pore throat changes. The contribution of particle rearrangement and mineral dissolution to the net structural changes, however, cannot be completely excluded. This process restructures the pore system of the ore body. Specifically, in the upper ore layer, loss of fine particles leads to increased pore count and porosity. The number of pore throats decreases, and the pore size distribution shifts toward smaller dimensions. In the lower layer, particle blockage reduces pore throat connectivity. These structural changes directly lower the overall solution seepage velocity. The velocity also decreases progressively with depth. Meanwhile, pore pressure is higher in the upper layer than in the lower layer. This creates a local pressure gradient. The gradient further promotes water infiltration into clay interlayers. It also accelerates fine particle detachment and migration. Ultimately, a coupled cycle forms among clay swelling, particle migration, and seepage weakening under laboratory column leaching conditions. The above mechanisms not only reduce rare earth recovery efficiency but also weaken the internal stability of the ore body, which may potentially contribute to landslide hazards when extrapolated to the field scale. The composite lixiviant (CDETA) and multiple characterization techniques used in this study provide useful guidance for evaluating microstructural evolution during leaching and its impact on seepage behavior.

Statement of the Use of Generative AI and AI-Assisted Technologies in the Writing Process

During the preparation of this manuscript, the author(s) used DeepSeek in order to improve the accuracy of English writing and check for grammatical errors. After using this tool, the author(s) reviewed and edited the content as needed and take(s) full responsibility for the content of the published article.

Author Contributions

Conceptualization, W.C.; Methodology, D.L.; Software, Y.R.; Validation, R.C., Z.C. and Z.Z.; Formal Analysis, W.C.; Investigation, Y.R.; Resources, R.C.; Data Curation, W.C.; Writing—Original Draft Preparation, W.C.; Writing—Review & Editing, Z.C.; Visualization, D.L.; Supervision, R.C., Z.Z. and S.L.; Project Administration, R.C.; Funding Acquisition, W.C. and Z.C.

Ethics Statement

Not applicable.

Informed Consent Statement

Not applicable.

Data Availability Statement

The data presented in this study are available on request from the corresponding author.

Funding

This research was funded by the National Natural Science Foundation of China (52504332, 52304293, U24A2096) and Open Project of Key Laboratory of Green Chemical Engineering Process of Ministry of Education (GCP2025001).

Declaration of Competing Interest

The authors declare that they have no known competing financial interests or personal relationships that could have appeared to influence the work reported in this paper.

References

1. Zhao M, Zhang H, Han H, Jiang X, Yang Y, Li T. Differential leaching mechanisms and ecological impact of organic acids on ion-adsorption type rare earth ores. *Sep. Purif. Technol.* **2025**, *362*, 131701. DOI:10.1016/j.seppur.2025.131701
2. Zhang Z, He Z, Xu Z, Yu J, Zhang Y, Chi R. Rare earth partitioning characteristics of China rare earth ore. *Chin. Rare Earths* **2016**, *37*, 121–127. DOI:10.16533/j.cnki.15-1099/tf.201601020
3. Chen W, Zhang Z, Long F, Chen Z, Chi R. Rare Earth Occurrence States of Weathered Crust Elution-Deposited Rare Earth Ores in Southern Yunnan. *Minerals* **2023**, *13*, 554. DOI:10.3390/min13040554
4. Chen Z, Zhang Z, Liu D, Chi X, Chen W, Chi R. Swelling of clay minerals during the leaching process of weathered crust elution-deposited rare earth ores by magnesium salts. *Powder Technol.* **2020**, *367*, 889–900. DOI:10.1016/j.powtec.2020.04.008
5. Guo D, Chen L, Zhou Z, Wang D, Zhang Y, Yang X, et al. Development of a pressure coring system for the investigation of deep underground exploration. *Int. J. Min. Sci. Technol.* **2023**, *33*, 1351–1364. DOI:10.1016/j.ijmst.2023.10.001
6. Guo Z, Liu L, Liu Y, Wu J, Wang X. Discussion on the Applicability and Landslide Prediction Method for Weathered Crust Elution-deposited Rare Earth Ore. *Chin. Rare Earths* **2025**, *46*, 111–125. DOI:10.3724/S1004-0277.20240067
7. Zhang L, Wen B, Chen L, Wang L. Variations in pore structures and permeabilities of the ion-adsorption rare earth ores in the zones with different weathering degree before and after leaching. *Hydrogeol. Eng. Geol.* **2024**, *51*, 117–124. DOI:10.16030/j.cnki.issn.1000-3665.202312048
8. Zhang Z, He Z, Zhou F, Zhong C, Sun N, Chi R. Swelling of clay minerals in ammonium leaching of weathered crust elution-deposited rare earth ores. *Rare Met.* **2018**, *37*, 72–78. DOI:10.1007/s12598-017-0977-7
9. Zhou L, Wang X, Huang C, Wang H, Ye H, Hu K, et al. Development of pore structure characteristics of a weathered crust elution-deposited rare earth ore during leaching with different valence cations. *Hydrometallurgy* **2021**, *201*, 105579. DOI:10.1016/j.hydromet.2021.105579
10. Luo S, Huang Q, Wang G, Hu S, Hong B. Permeability change rule of ion-adsorption rare-earth in ore leaching process. *Nonferrous Met. Sci. Eng.* **2014**, *5*, 95–99. DOI:10.13264/j.cnki.ysjskx.2014.02.017
11. Wang X, Zhuo Y, Deng S, Li Y, Zhong W, Zhao K. Experimental Research on the Impact of Ion Exchange and Infiltration on the Microstructure of Rare Earth Orebody. *Adv. Mater. Sci. Eng.* **2017**, *2017*, 4762858. DOI:10.1155/2017/4762858
12. Dianyu E, Su Z, Zeng J, Yang L, Li J, Xu Q, et al. Numerical Study of Percolation and Seepage Behaviors in Ion-Adsorption-Type Rare Earth Ore Leaching Process. *Math. Probl. Eng.* **2023**, *2023*, 5916294. DOI:10.1155/2023/5916294
13. Liu J, Wang R, Song P, Li Y, Zheng S. Quantitative Characterization and Flow Simulation of Micropore Structure in Clastic Gas Reservoirs Based on Micron CT Scanning. *ACS Omega* **2025**, *10*, 20686–20700. DOI:10.1021/acsomega.5c01569
14. Liu X, Zhu H, Liang L. Digital rock physics of sandstone based on micro-CT technology. *Chin. J. Geophys.* **2014**, *57*, 1133–1140. DOI:10.6038/cjg20140411
15. Qi C, Wang X, Wang W, Liu J, Tuo J, Liu K. Three-dimensional fine characterization method of micro-fractures in shale reservoirs. *Acta Pet. Sin.* **2018**, *39*, 1175–1185. DOI:10.7623/syxb201810009
16. Liu X, Xiong J, Liang L, Yang W. Study on the characteristics of pore structure of tight sand based on micro-CT scanning and itsinfluence on fluid flow. *Prog. Geophys.* **2017**, *32*, 1019–1028. DOI:10.6038/pg20170310
17. Yin S, Chen X, Yan R, Wang L. Pore Structure Characterization of Undisturbed Weathered Crust Elution-Deposited Rare Earth Ore Based on X-ray Micro-CT Scanning. *Minerals* **2021**, *11*, 236. DOI:10.3390/min11030236
18. Li G, Dai S, Zhan L, Chen Y. A pore-scale numerical investigation of the effect of pore characteristics on flow properties in soils. *J. Zhejiang Univ. Sci. A* **2019**, *20*, 961–978. DOI:10.1631/jzus.A1900255
19. Zhuo Y, Wang X, Cao S, Deng S, Li Y, Han J. Study on relationship between pore structure and strengthweakening of rare earth ore under seepage. *Gold Sci. Technol.* **2017**, *25*, 101–106. DOI:10.11872/j.issn.1005-2518.2017.05.101

20. Liu D, Zhang Z, Chi R, Xi Y, Yan S. Experimental study on the influence of particle size on the strength characteristics of weathered crust elution-deposited rare earth ores. *Nonferrous Met. Eng.* **2020**, *10*, 97–103. DOI:10.3969/j.issn.2095-1744.2020.06.015
21. Fredlund D. Myths and misconceptions related to unsaturated soil mechanics. *Soils Rocks* **2021**, *44*, e2021062521. DOI:10.28927/SR.2021.062521
22. Chen X, Yin S, Yan R, Wang L. Evolution characteristics of mesoscopic pore structure of weathered crust elution deposited rare earth ore under solution seepage. *Chin. J. Eng.* **2021**, *43*, 1283–1294. DOI:10.13374/j.issn2095-9389.2021.02.24.003
23. Liu D, Yan W, Zhang Z, Guo W, Chi R. Study on Continuously Weakening Mechanism of Heap Leaching Velocity of Weathered Rare Earth Ores with the Increase of Ore Burial Depth. *Minerals* **2023**, *13*, 581. DOI:10.3390/min13040581
24. Liu R, Li B, Jiang Y, Yu L. Effects of equivalent hydraulic aperture and hydraulic gradient on nonlinear seepage properties of rock mass fracture networks. *Rock Soil Mech.* **2016**, *37*, 3165–3174. DOI:10.16285/j.rsm.2016.11.016
25. Wang G, Wang X, Hu S, Hong B. Experimental study on the effect of particle migration on the structure of ionic rare earth ore body. *Min. Res. Dev.* **2015**, *35*, 37–42. DOI:10.13827/j.cnki.kyyk.2015.10.009
26. Wang X, Li Y, Huang G, Fang S, Zhong W, Liao S. Research of permeability and porosity in ion-type rare earth leaching process. *Chin. Rare Earths* **2017**, *38*, 47–55. DOI:10.16533/j.cnki.15-1099/tf.201705007
27. Chang B, Du C, Sun M, Lin Y, Wang Y, Chu X, et al. Mesoscopic Seepage Simulation and Analysis of Unclassified Tailings Pores Based on 3D Reconstruction Technology. *ACS Omega* **2021**, *6*, 14309–14316. DOI:10.1021/acsomega.1c01092
28. Gomes R, Bradford SA, Sasidharan S. Vadose zone infiltration wells for stormwater management and managed aquifer recharge: A global review and pre-/post-installation decision framework. *Crit. Rev. Environ. Sci. Technol.* **2026**, *56*, 886–907. DOI:10.1080/10643389.2026.2678936